Magnetic Resonance Imaging 131 (2026) 110696

Contents lists available at ScienceDirect

Magnetic Resonance Imaging

journal homepage: www.elsevier.com/locate/mri

A mathematically accurate angular regression model optimizes phase activation and yields additional physiological information in FMRI

John C. Bodenschatz, Daniel B. Rowe *

Department of Mathematical and Statistical Sciences, Marquette University, 1313 W. Wisconsin Avenue, Milwaukee, 53233, WI, USA

ARTICLE INFO

Keywords:
FMRI
MLE
Phase
Activation

ABSTRACT

In functional magnetic resonance imaging (fMRI), it is important to observe the functioning brain as fast as possible and at as high of a spatial resolution as possible. Increased spatial and temporal speed results in voxels with increased noise relative to signal and contrast. There is much evidence to suggest that there is important biological information contained within the phase component of the fMRI signal. When the signal-to-noise ratio within a voxel is low, as when there is ultra-high resolution, the marginal statistical distribution of the phase is non-standard and difficult to work with. This non-standard marginal phase distribution at high signal-to-noise ratios is Normally distributed, but at low signal-to-noise ratios needs to be utilized for accurate modeling. In this work, phase-only activation will be computed directly from Lathi's mathematically correct non-Normal distribution, yielding additional physiological information to what is typically observed.

1. Introduction

In functional magnetic resonance imaging (fMRI), images are most often collected via single shot echo planar imaging (EPI). The most commonly used pulse sequence in EPI for fMRI is gradient recalled echo (GRE) [1,2]. The steady state GRE signal equation, given by

$$s(k_x, k_y) = \int_{-\infty}^{\infty}\int_{-\infty}^{\infty} \frac{M_0 \sin(\alpha)}{\left(1-\cos(\alpha)e^{-TR/T_1}\right)} \times \left(1-e^{-\mathrm{TR}/T_1}\right) e^{-t/T_2^*} e^{i\gamma \Delta B t} e^{-i2\pi(k_x x + k_y y)}\, dx\, dy, \tag{1}$$

yields a complex-valued signal s at a given point (k_x, k_y) in k-space. A point of interest in the GRE signal equation is the term $e^{i\gamma \Delta B t}$ where ΔB is a catch-all term for any spatio-temporal inhomogeneity in the magnetic field local to a voxel. These fluctuations from the intended uniform magnetic field can be caused by scanner imperfections, gradient coil imperfections and eddy currents, patients' own magnetization, tissue composition and interfaces with air, and more [2–4]. Since the exponential term that includes ΔB is the only non-Fourier term that includes an imaginary part, the local biological information contained within ΔB can be found within the local phase of reconstructed images. It is often the case that the true complex-valued nature of fMRI data is ignored, and only magnitude images are studied.

In fMRI, the blood-oxygen-level-dependent (BOLD) signal is interrogated to determine regions of activation [5,6]. The BOLD signal is a measure of localized brain blood volume and oxygenation changes which are correlates for neuronal activity. These changes occur as a result of certain stimuli or tasks, e.g., right-hand finger tapping, that activate known regions of the brain. The BOLD signal presents itself as a T_2^* effect since the change in magnetic properties of oxygenated and deoxygenated hemoglobin in blood causes a perturbation in the local magnetic field, ΔB, which causes a transverse dephasing of spins. Hence, fMRI time series are T_2^*-weighted images, highlighting regions of the brain with significant T_2^* effects. It is known that

$$1/T_2^* = 1/T_2 + 1/T_2' \tag{2}$$

where T_2 is the "true" transverse relaxation effect due to intrinsic molecular interactions, and T_2' is transverse relaxation due to magnetic field inhomogeneities ΔB. In fact, $1/T_2' = \gamma \Delta B$ which is located in the non-Fourier complex exponential term in Eq. (1) [7]. The BOLD signal has a measurable effect in both the magnitude (from the term e^{-t/T_2^*}) and phase (from the term $e^{i\gamma \Delta B t}$) of the signal within a voxel. Therefore one would expect to observe any detectable task-related signal change within a voxel in both the magnitude and phase of the reconstructed voxel time series. Traditionally the BOLD signal is analyzed in magnitude-only images, discarding any information contained within the phase. It is possible that there is change in one or both of the magnitude and phase [8]. If the phase data is ignored, only changes in magnitude can be detected, which leads to the loss of physiological information found in the phase.

Historically in fMRI, a general linear model with Normally distributed errors was used for the marginal distribution of the magnitude

---

* Corresponding author.
E-mail address: daniel.rowe@marquette.edu (D.B. Rowe).

https://doi.org/10.1016/j.mri.2026.110696
Received 13 February 2026; Received in revised form 22 April 2026; Accepted 22 April 2026

component of the time series [6]. However, the Normal assumption is not valid at low signal-to-noise ratios (SNRs). Recently, efforts have been made to use the proper Ricean marginal distribution for the magnitude component in fMRI [9–11]. It should be noted that there is also a line of research utilizing the full complex-valued time series [8,12–15]. In this line of research, task related magnitude, phase, or magnitude and phase activation is computed within the full complex-valued time series. It is believed that by using the full $2n$ complex-valued measurements there is increased detection power over using n magnitude measurements even at high SNR [9]. Further, when there are task related changes in both the magnitude and phase, a model that detects both yields increased detection of task activation [8]. Ever increasing relaxation of the assumed model parameters was made [11,16,17] as well as Bayesian inference [18–21]. There has been some effort to properly estimate and perform inferences on the phase component of the time series [22]. In past work, researchers centered each voxel time series, unwrapped it, and simply fit a linear regression model with Normally distributed errors. However this can have challenges when there are one or more phase transitions on the $[-\pi, \pi]$ boundary and Type I and II errors when the incorrect distribution is used. In this work, we will use Lathi's mathematically correct phase distribution to compute task-related phase activation [23]. This will be compared to using a Normal distribution and a more accurate angular regression model to make estimations [22].

2. Methods

2.1. Distributions

It has been well established that MRI voxel values are complex-valued consisting of real and imaginary parts. The real y_R and imaginary y_I parts of a given voxel value at a specified time contain independent additive Normally distributed noise, $y_R \sim N(\rho\cos\theta, \sigma^2)$ and $y_I \sim N(\rho\sin\theta, \sigma^2)$ [24–26]. The parameters ρ and θ represent the true magnitude and phase signal within the voxel. The joint distribution of the real and imaginary parts can be expressed as a bivariate Normal distribution with phase-coupled means

$$f(y_R, y_I|\rho, \theta, \sigma^2) = \frac{1}{(2\pi\sigma^2)^{1/2}} \exp\left[-\frac{(y_R - \rho\cos(\theta))^2}{2\sigma^2}\right] \times \frac{1}{(2\pi\sigma^2)^{1/2}} \exp\left[-\frac{(y_I - \rho\sin(\theta))^2}{2\sigma^2}\right]. \tag{3}$$

A transformation of variables from the Cartesian random variables (y_R, y_I) to the polar random variables (r, ϕ) can be performed, resulting in the following joint distribution for the measured magnitude r and phase ϕ

$$f(r, \phi|\rho, \theta, \sigma^2) = \frac{r}{2\pi\sigma^2} \exp\left[-\frac{1}{2\sigma^2}\left[r^2 + \rho^2 - 2r\rho\cos(\phi - \theta)\right]\right]. \tag{4}$$

From this bivariate distribution, the Ricean marginal distribution for magnitude with location ρ and scale σ can be extracted by integrated out the phase ϕ, yielding

$$f(r|\rho, \sigma^2) = \frac{r}{\sigma^2} \exp\left[-\frac{r^2 + \rho^2}{2\sigma^2}\right] I_0\left(\frac{r\rho}{\sigma^2}\right) \tag{5}$$

where I_0 is the zeroth order modified Bessel function of the first kind [14,25,27]. The mathematically correct marginal distribution for phase, which will further be referred to as the "Lathi" distribution, is found to be

$$f(\phi|\rho, \theta, \sigma^2) = \frac{1}{2\pi} \exp\left[-\frac{\rho^2}{2\sigma^2}\right] \times \left[1 + \frac{\rho}{\sigma}\sqrt{2\pi}\cos(\phi - \theta)\exp\left[\frac{\rho^2\cos^2(\phi - \theta)}{2\sigma^2}\right] \Phi\left(\frac{\rho\cos(\phi - \theta)}{\sigma}\right)\right], \tag{6}$$

where $\Phi(x)$ is the cumulative distribution function of the standard Normal distribution [14,23,28]. This Lathi distribution is often approximated to be the Normal distribution. This approximation is only supported in voxels where the true signal ρ is high relative to the noise σ. The von Mises distribution, a close approximation to the wrapped Normal distribution, has also been used to characterize the phase [22]. In regions of empty space where $\rho \approx 0$, the Lathi distribution becomes uniform on the interval $[-\pi, \pi]$. A power analysis of the distribution in Eq. (6) compared to the Normal and von Mises approximations as well as a visual comparison of the three distributions are explored in Appendix A. At a fixed Type I error rate of $\alpha = 0.05$, the Lathi distribution provides the largest statistical power over the Normal and von Mises distributions, indicating an increased ability to correctly identify task-active voxels.

2.2. Estimation

In fMRI, there is a time series of n complex-valued measurements collected at each voxel location. An association measure between the time series and the expected response from the fMRI experiment is computed, usually in the form of a linear regression that is applied to only the magnitude of the complex-valued time series. Without task, the parameters in Eq. (5) can be estimated via maximum likelihood estimation. The likelihood function is given by

$$L(\rho, \sigma^2) = \prod_{t=1}^{n} f(r_t|\rho, \sigma^2), \tag{7}$$

where $f(r_t|\rho, \sigma^2)$ is the Ricean distribution described in Eq. (5).

Similarly, without task, the parameters in Eq. (6) can be estimated via maximum likelihood estimation. The likelihood function is given by

$$L(\rho, \theta, \sigma^2) = \prod_{t=1}^{n} f(\phi_t|\rho, \theta, \sigma^2), \tag{8}$$

with $\theta = \theta_0$ where θ_0 is the baseline phase. In the case where task is present, $\theta = \theta_0 + \theta_1 x_t$ where θ_1 is the additive task-related signal and $x_t \in \{0, 1\}$ is an indicator of expected response at time t.

This can be structured as a hypothesis test of $H_0 : \theta_1 = 0$ versus $H_1 : \theta_1 \neq 0$. The likelihood for the null and alternative hypotheses can be maximized and the parameters estimated via maximum likelihood estimation (MLE). Since it is well known that the task-related magnitude signal change is extremely small compared to the baseline, an aggregated magnitude MLE $\hat{\rho}$ is used when computing the phase MLEs from Eq. (8). This also provides an estimate for $\hat{\sigma}^2$ which is updated during the phase estimation.

Utilizing the distribution in Eq. (6) for each of the n observations at time t, the phase likelihood becomes

$$L(\theta, \sigma^2) = \prod_{t=1}^{n} \left\{ \frac{1}{2\pi} \exp\left(-\frac{\hat{\rho}^2}{2\sigma^2}\right) \left[1 + \frac{\hat{\rho}}{\sigma}\sqrt{2\pi}\cos(\phi_t - \theta)\exp\left(\frac{\hat{\rho}^2\cos^2(\phi_t - \theta)}{2\sigma^2}\right) \Phi\left(\frac{\hat{\rho}\cos(\phi_t - \theta)}{\sigma}\right)\right]\right\} \tag{9}$$

where $\theta = \theta_0$ under the null hypothesis and $\theta = \theta_0 + \theta_1 x_t$ under the alternative hypothesis. A grid search for the parameters the maximum likelihood estimates was also performed and results are consistent with the optimization procedures used.

A voxel-wise likelihood ratio statistic $\lambda = L_{H_0}/L_{H_1}$ can be computed as the ratio of the null likelihood over the alternative likelihood, and the $\Lambda = -2\ln(\lambda) \sim \chi^2(1)$ test statistic formed [29]. Since there is a single degree of freedom, a z-statistic can be formed

$$z = \text{sign}(\hat{\theta}_1)\sqrt{-2\ln(\lambda)} \tag{10}$$

and utilized to detect "task-active" voxels [30].

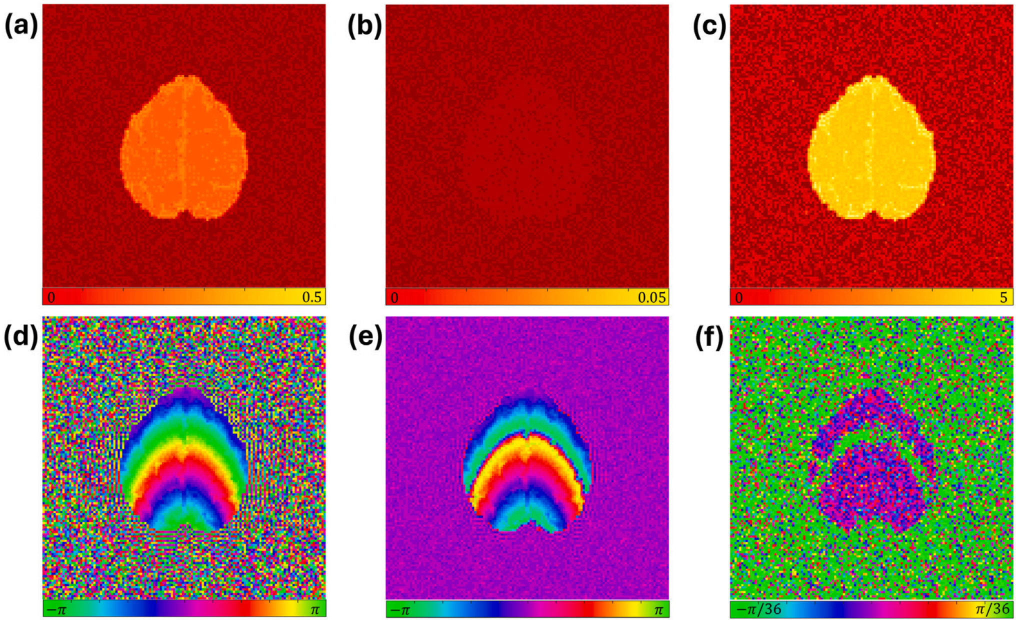

Fig. 1. Maximum likelihood estimation for $\hat{\rho}$ (a) and $\hat{\sigma}^2$ (b) from Eq. (7) with resulting SNR (c). Average angular measured voxel phase $\bar{\phi}$ (d). Linear regression estimate for $\hat{\theta}_0$ (e) and $\hat{\theta}_1$ (f). Notice the within brain banding effect in (f) that is a result of phase wrap-around. This can make diagnosing regions that contain task-related activity difficult.

3. Results

3.1. Simulated results

This method was tested on both simulated and experimental fMRI data. The simulated data was made using the same MR parameters as the experimental data for consistency of methods and comparability of results. The simulated fMRI time series data was generated using SHAKER v1.1 [31]. The simulated time series is of slice 91 from a size 128 phantom in the Axial plane. The MRI parameters were set to be the following: Acceleration Factor = 1, Field Strength = 3 T, TE = 50 ms, TR = 1000 ms, Flip Angle = 90°, EESP = 0.832 ms, and Number of Coils = 1. The data was simulated with the Gradient Echo signal equation (Eq. (1)) using a Cartesian k-space trajectory. The experimental design involved an initial 16 rest images followed by 19 epochs, each consisting of 16 task images followed by 16 rest images, for a total of 624 images. The initial 3 images are omitted from analysis. The SNR was set to be about 5 in the brain and the CNR was set to 0.25 in the region of task-activation. There were 6 degrees of phase added to the region of activation.

Fig. 1 are voxel-wise estimates that use the Normal distribution ordinary least squares (OLS) and not the Lathi distribution in Eq. (6). Figs. 1(a) and 1(b) depict the MLE estimates for magnitude and variance from Eq. (7). Fig. 1(c) shows the estimated SNR defined by $\widehat{SNR} = \hat{\rho}/\hat{\sigma}$, which was intentionally simulated to be about 5 within the brain. Fig. 1(d) depicts the mean angular phase $\bar{\phi}$ of the time series. Figs. 1(e) and 1(f) are the simple linear regression coefficient estimates for baseline phase θ_0 and task-related phase θ_1. The baseline phase coefficient estimate appears reasonable within the brain when compared to the mean angular phase, but poorly estimates the regions in empty space. Similarly, the task related phase coefficient estimate is very unreasonable in empty space, and within the brain there is a very clear banding artifact that comes from the phase wraparound near the $[-\pi, \pi]$ boundary. This artifact can make it very difficult to determine with confidence both the existence of task-related phase change and the true value of the angular difference from baseline phase.

Another phase model described by Rowe (2007) uses the von Mises distribution to characterize the phase. This distribution has support on $[-\pi, \pi]$ and is often compared to the wrapped Normal distribution. The results of applying this model to the simulated data under the alternative hypothesis are shown in Fig. 2. The baseline phase estimate $\hat{\theta}_0$ (a) is spatially smoother at the wraparound regions, and the estimate for task-related phase change $\hat{\theta}_1$ is free of the banding artifacts that were observed with Normal estimation. The variance of estimation is increased, largely in regions of empty space.

Fig. 3 shows the maximum likelihood estimates of $\hat{\theta}_0$, $\hat{\sigma}^2$, and $\hat{\theta}_1$ under the null and alternative hypothesis in the top and bottom rows respectively. Contrary to Fig. 1, these estimations are based on the more accurate Lathi distribution in Eq. (6) and formed via the maximum likelihood presented in Eq. (9). In the top row, Figs. 3(a) and 3(b) depict the estimates $\hat{\theta}_0$ and $\hat{\sigma}^2$ under the null hypothesis that $\theta = \theta_0$. In the bottom row, Figs. 3(d), 3(e), and 3(f) depict the estimates $\hat{\theta}_0$, $\hat{\theta}_1$, and $\hat{\sigma}^2$ under the alternative hypothesis that $\theta = \theta_0 + \theta_1 x_t$. The estimate $\hat{\theta}_0$ is approximately the same for both hypotheses while the estimate for $\hat{\sigma}^2$ appears to be slightly decreased in empty space under the alternative hypothesis. The estimate for $\hat{\theta}_1$ looks nearly uniform at about 0 inside the brain, and noisy in empty space.

While the image of $\hat{\theta}_1$ in Fig. 3(e) appears fairly spatially smooth just like with the simulated data in Fig. 2, closer examination reveals details about the nature of θ_1. Calculating the likelihood ratio statistic as described in Section 2.2 and corresponding z-statistic as described by Eq. (10), we can highlight exactly where the task-related phase coefficient θ_1 is significant. The z-statistics produced from this method, presented in Fig. 4, are thresholded using the Benjamini–Hochberg procedure to control the false discovery rate at the $\alpha = 0.05$ level [32–34]. The resultant critical z-statistics are found to be ±3.28, ±4.40, and ±4.45 for the Normal, von Mises, and Lathi distributions, respectively. Here we can clearly identify a region of task-related phase change. The average value for $\hat{\theta}_1$ in the voxels that were simulated to have an additional 6 degrees of task-related phase change was found to be 5.34 degrees. In each of Figs. 1(f), 2(b), and 3(f), the measure for $\hat{\theta}_1$ is a direct measure of the change in magnetic field local to the space that make up each of the voxels.

3.2. Experimental results

Experimental data is from a single subject block design right-hand finger tapping experiment on a 3.0-Tesla General Electric Signa LX MRI

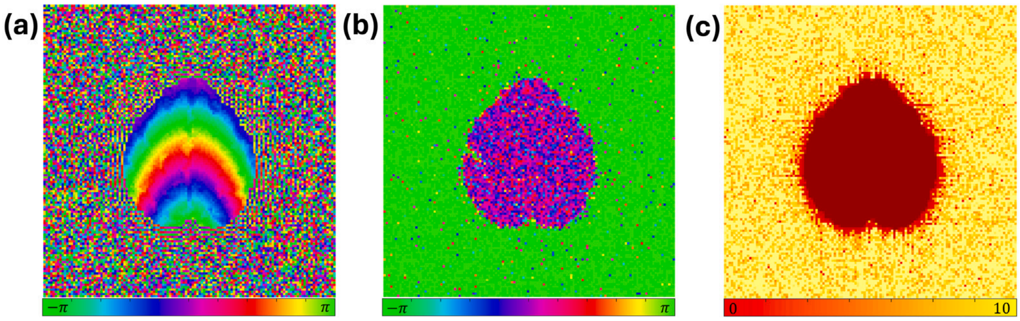

Fig. 2. Simulated data estimations from the von Mises approximation for $\hat{\theta}_0$ (a), $\hat{\theta}_1$ (b), and $\hat{\sigma}^2$(c) under the alternative hypothesis, $\theta = \theta_0 + \theta_1 x_t$. Note the high scale of variance in space compared to the Normal distribution in Fig. 1 and later for the Lathi distribution in Fig. 3.

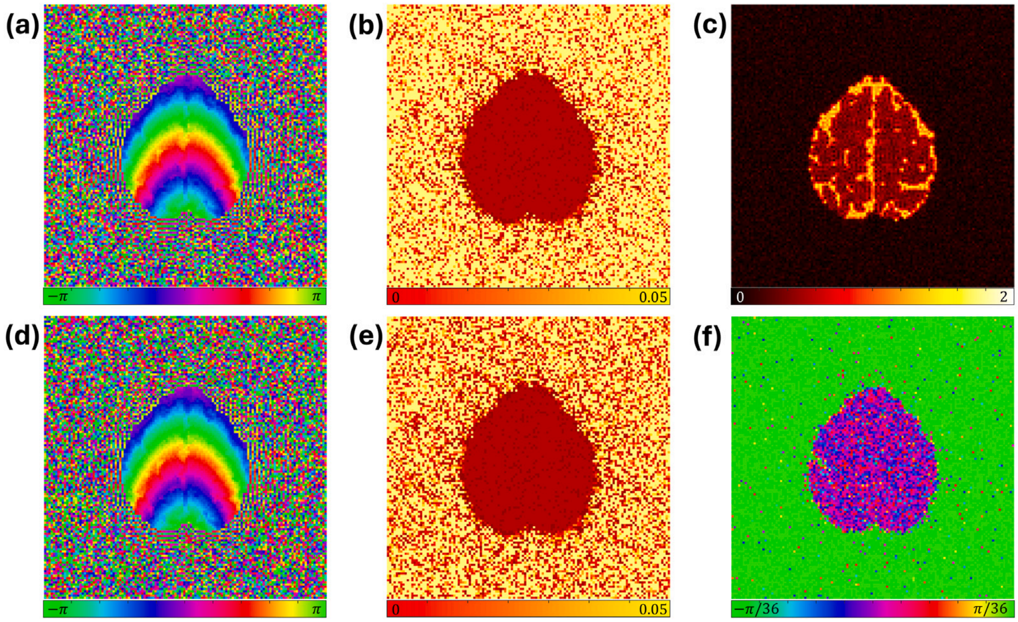

Fig. 3. Maximum likelihood estimations for $\hat{\theta}_0$ (a) and $\hat{\sigma}^2$ (b) under the null hypothesis, $\theta = \theta_0$ with anatomical image (c). Maximum likelihood estimations for $\hat{\theta}_0$ (d), $\hat{\sigma}^2$ (e), and $\hat{\theta}_1$ (f) under the alternative hypothesis, $\theta = \theta_0 + \theta_1 x_t$.

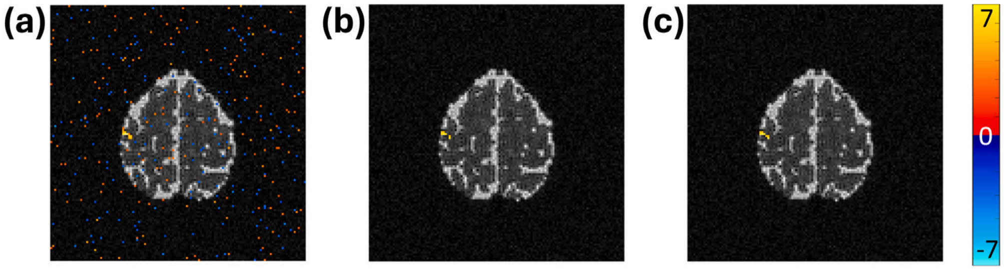

Fig. 4. Z-statistics from each of the three distributions, thresholded by the Benjamini–Hochberg procedure controlling the false discovery rate at the $\alpha = 0.05$ level. The results from the Normal approximation (a), von Mises approximation (b), and mathematically correct Lathi distribution (c). The Lathi distribution was most successful in determining task-active voxels.

scanner. The imaging parameters were n_z=7 slices of 2.5 mm thick and 128 × 128 array size with a field-of-view FOV=24.0 cm, echo time TE=60.4 ms, effective echo spacing EESP=0.832 ms, and time-of-repetition TR=1 s. The experiment timing followed an initial 16 s of rest followed by 19 epochs of 16 s of task alternating with 16 s of rest resulting in a total of n_t=624 total image volumes. The initial 3 images are omitted from analysis. Each slice image at each time point, was Nyquist ghost corrected [35]. Images were phase drift corrected by subtracting each voxel's angular phase temporal mean. A local second order polynomial was spatially fit to the resultant difference of each phase image in the time-series. The spatially fitted phase is angularly subtracted from the original time series [36]. A simple linear regression model was fit to each voxel's unwrapped phase time series and angularly subtracted off. Then the angular mean was added to each voxel's time series, resulting in a stable global phase over time.

Fig. 5 are voxel-wise estimates that use the Normal distribution OLS and not the Lathi distribution in Eq. (6); this figure is the experimental equivalent to Fig. 1. Figs. 5(a) and 5(b) depict the MLE estimates for magnitude and variance from Eq. (7). Fig. 5(c) shows the SNR which was found to be about 5 within the brain. These brain images were

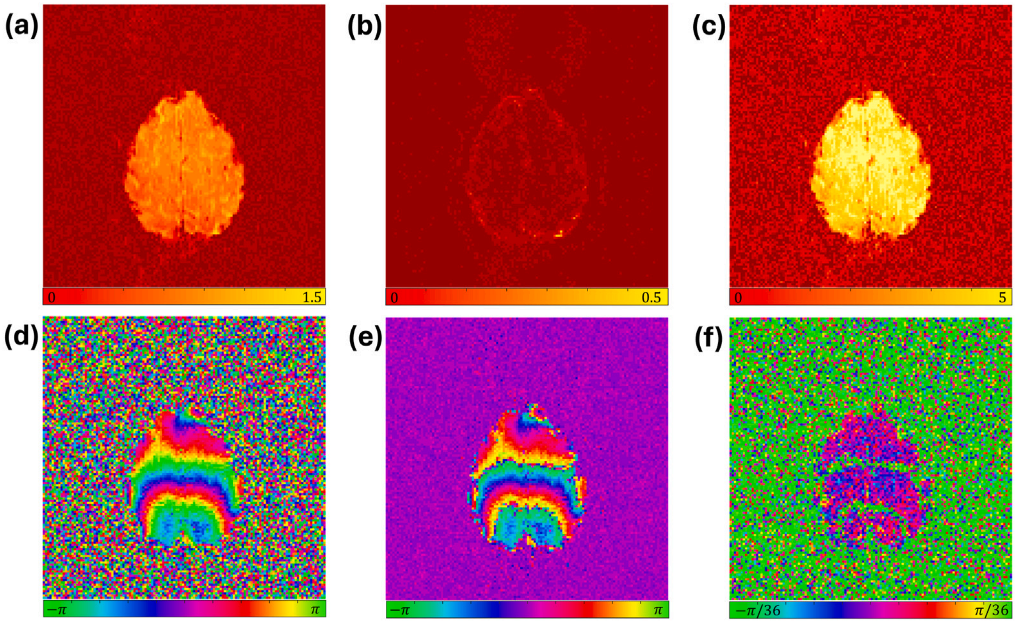

Fig. 5. Maximum likelihood estimation for $\hat{\rho}$ (a) and $\hat{\sigma}^2$ (b) from Eq. (7) with resulting SNR (c). Average angular measured voxel phase $\bar{\phi}$ (d). Linear regression estimate for $\hat{\theta}_0$ (e) and $\hat{\theta}_1$ (f). Notice the within brain banding effect in (f) that is a result of phase wrap-around. This can make diagnosing regions that contain task-related activity difficult.

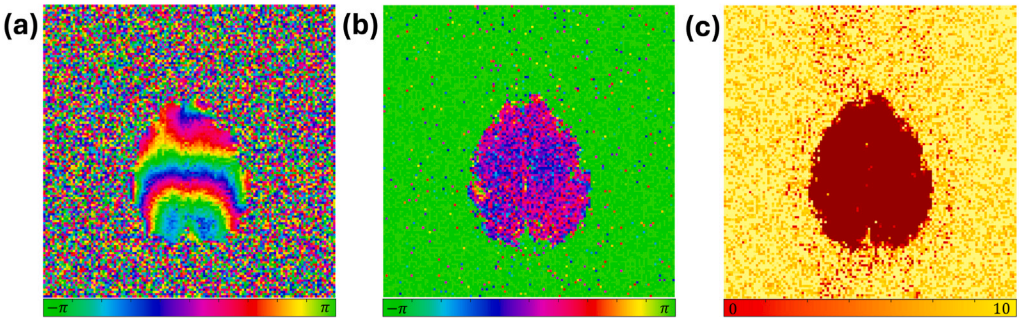

Fig. 6. Experimental data estimations from the von Mises approximation for $\hat{\theta}_0$ (a), $\hat{\theta}_1$ (b), and $\hat{\sigma}^2$(c) under the alternative hypothesis, $\theta = \theta_0 + \theta_1 x_t$. Note the high scale of variance in space compared to the Normal distribution in Fig. 5 and later for the Lathi distribution in Fig. 7.

collected using a body receive coil with decreased SNR, resulting in particularly noisy data. Fig. 5(d) depicts the mean angular phase $\bar{\phi}$ of the experimental time series. Figs. 5(e) and 5(f) are the simple linear regression coefficient estimates for baseline phase θ_0 and task-related phase θ_1. Similar to the simulated data, the baseline phase coefficient estimate appears reasonable within the brain when compared to the mean angular phase, but poorly estimates the regions in empty space. Also the task related phase coefficient estimate is very unreasonable in empty space, and within the brain there is a very clear banding artifact that comes from the phase wraparound near the $[-\pi, \pi]$ boundary. This artifact makes it impossible to determine with confidence the existence of task-related phase change.

The results of applying the previously described von Mises model to the experimental data under the alternative hypothesis are shown in Fig. 6 [22]. Similarly to the simulated data, we see improved estimation of both the baseline phase and task-related phase change. The results are more consistent with what we would expect based on the mean angular phase $\bar{\phi}$.

Fig. 7 shows the maximum likelihood estimates of $\hat{\theta}_0$, $\hat{\sigma}^2$, and $\hat{\theta}_1$ under the null and alternative hypothesis in the top and bottom rows respectively; this is the experimental equivalent of Fig. 3. In the top row, Figs. 7(a) and 7(b) depict the estimates $\hat{\theta}_0$ and $\hat{\sigma}^2$ under the null hypothesis that $\theta = \theta_0$. In the bottom row, Figs. 7(d), 7(e), and 7(f) depict the estimates $\hat{\theta}_0$, $\hat{\theta}_1$, and $\hat{\sigma}^2$ under the alternative hypothesis that $\theta = \theta_0 + \theta_1 x_t$. The estimate $\hat{\theta}_0$ is approximately the same for both hypotheses while the estimate for $\hat{\sigma}^2$ appears to be slightly decreased in empty space under the alternative hypothesis. The estimate for $\hat{\theta}_1$ looks mostly uniform at about 0 inside the brain and noisy in empty space, as one might expect.

The z-statistics produced from the method described in Section 2.2, presented in Fig. 8, are thresholded using the Benjamini–Hochberg procedure to control the false discovery rate at the $\alpha = 0.05$ level. The resultant critical z-statistics are found to be ±3.18, ±4.1, and ±3.89 for the Normal, von Mises, and Lathi distributions, respectively. The left motor cortex is expected to have a task-related signal change as a result of right-hand finger tapping (the performed task for the experimental data). There is a distinct region of voxels that have task-related phase increase exactly at this location. The average value for $\hat{\theta}_1$ in the voxels that were determined to have task-related phase change was found to be 6.33 degrees. In each of Figs. 5(f), 6(b), and 7(f), the measure for $\hat{\theta}_1$ is a direct measure of the change in magnetic field local to the space that make up each of the voxels.

An experimental signal time series selected from voxels in the left and right motor cortices as well as from the posterior midline are presented in Fig. 9 (center). A stable magnitude and phase are seen through time for both voxels (left). Neither the observed task-related

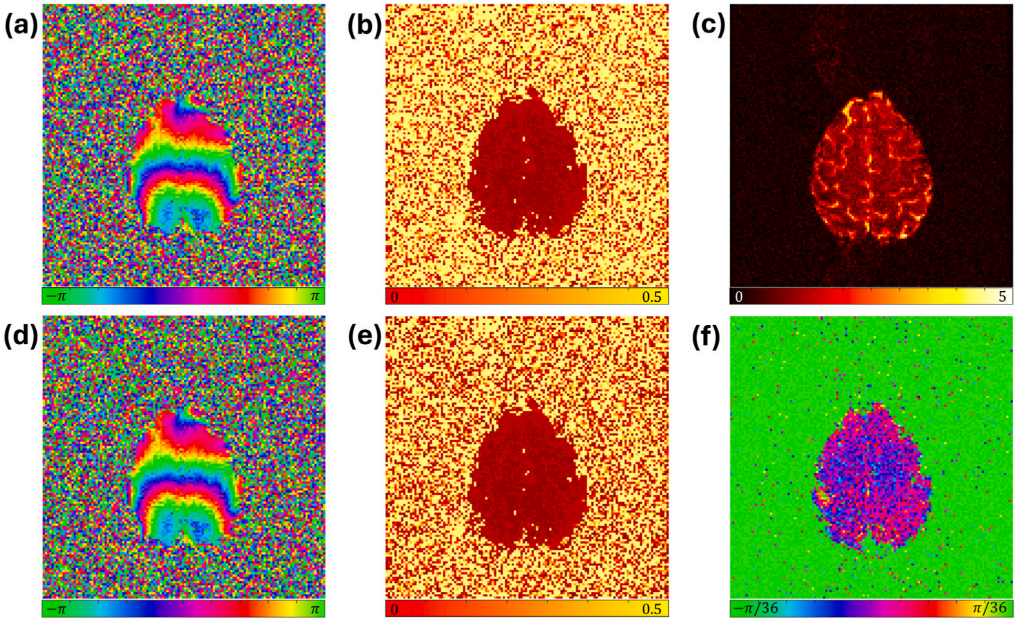

Fig. 7. Maximum likelihood estimations for $\hat{\theta}_0$ (a) and $\hat{\sigma}^2$ (b) under the null hypothesis, $\theta = \theta_0$ with anatomical image (c). Maximum likelihood estimations for $\hat{\theta}_0$ (d), $\hat{\sigma}^2$ (e), and $\hat{\theta}_1$ (f) under the alternative hypothesis, $\theta = \theta_0 + \theta_1 x_t$.

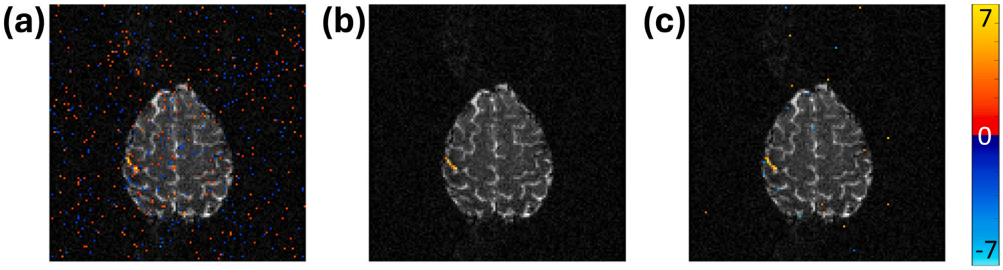

Fig. 8. Z-statistics from each of the three distributions, thresholded by the Benjamini–Hochberg procedure controlling the false discovery rate at the $\alpha = 0.05$ level. The results from the Normal approximation (a), von Mises approximation (b), and mathematically correct Lathi distribution (c). The Lathi distribution was most successful in determining task-active voxels.

phase change nor any task-related magnitude change are visually evident from the time series alone without further investigation. The gray shaded regions in the plots indicate TRs of subject task activation. The task-associated signal change is very small for both the magnitude and phase, making it difficult to visually infer from the time series alone. The magnitude (left) and phase (right) FDR thresholded z-statistics are shown as well as the locations of the selected voxels. The magnitude activation statistics are found from a magnitude-only model and thresholded to control the FDR at 0.05 [9].

The logarithm of the amplitudes of the Fourier coefficients of the Fourier transformed magnitude and phase time series from the same voxels in Fig. 9 are presented in Fig. 10. The zero-frequency has been omitted to further illustrate the differences between higher frequencies. The arrow in the top center plot for the voxel in the left motor cortex indicates a large Fourier coefficient at a frequency of about 0.03 Hz or 19/621 s^{-1}. The experimental timing had 19 epochs of the task on–off sequence that repeated every 32 s. No large Fourier coefficients are observed in the expected range for respiration (0.2–0.4 Hz). The TR of 1 s for the experimental data is consistent with fMRI experiments. As a result of the Nyquist criterion, any phenomenon occurring at a frequency greater than 0.5 Hz is unable to be isolated (e.g. cardiac rhythms in the 1–1.5 Hz range). The magnitude (left) and phase (right) FDR thresholded F-statistics for the Fourier coefficient at the previously mentioned 0.03 Hz are shown as well as the locations of the selected voxels. The F-statistics are computed by comparing the zero-frequency only model with a Fourier regression model. At each frequency, the F statistic is computed by

$$F_{2,n_t-2-1} = \frac{(RSS_1 - RSS_2)/2}{RSS_2/(n_t - 2 - 1)},$$

where RSS_1 is the residual sum of squares for the zero-frequency only model and RSS_2 is the residual sum of squares for the Fourier model that includes coefficients for specified, measurable frequencies. The F-statistics are thresholded at the $\alpha = 0.05$ level of significance. As indicated by the left and right figures, the time series for voxels in the left motor cortex were found to have statistically significant Fourier coefficients at a frequency of about 0.03 Hz.

4. Discussion

It is rarely the case in fMRI studies that the whole complex-valued data is studied, leaving out the phase information to look only at the magnitude data. Further, when phase data *is* analyzed, the time series distribution of measurements is often simplified to the Normal distribution, which is only valid in voxels with high SNR. The Normal distribution also lacks support on the unit circle in favor of the real line, which creates artifacts when the measured phase is near the $[-\pi, \pi]$ boundary. In this work the mathematically correct non-Normal distribution from Lathi, which is valid for all SNRs, was used to estimate task-related changes in the phase signal. This maximum likelihood

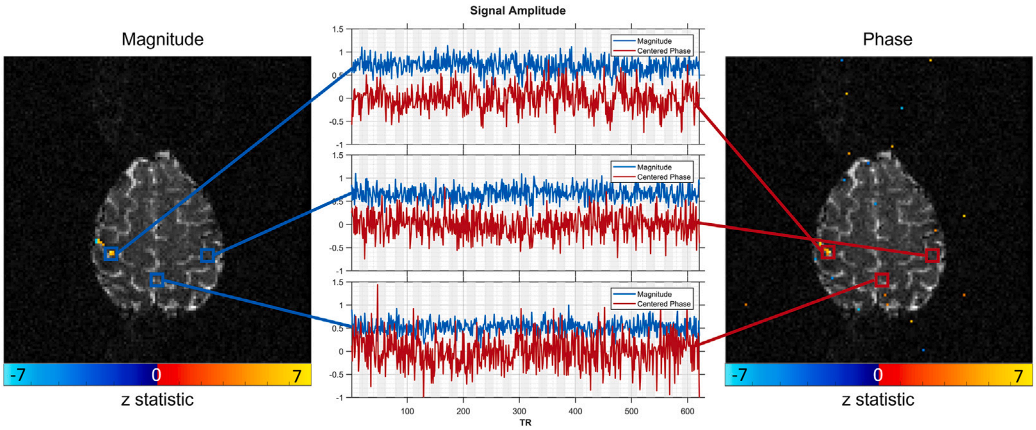

Fig. 9. Experimental data time series (center) of the magnitude (blue) and phase (red) of voxels located in the left motor cortex (top), right motor cortex (bottom), and posterior midline (bottom). The gray shaded regions in the time series plots indicate TRs of subject task activation. Left and right are the significant z-statistics for magnitude- and phase-only activation, respectively. (For interpretation of the references to color in this figure legend, the reader is referred to the web version of this article.)

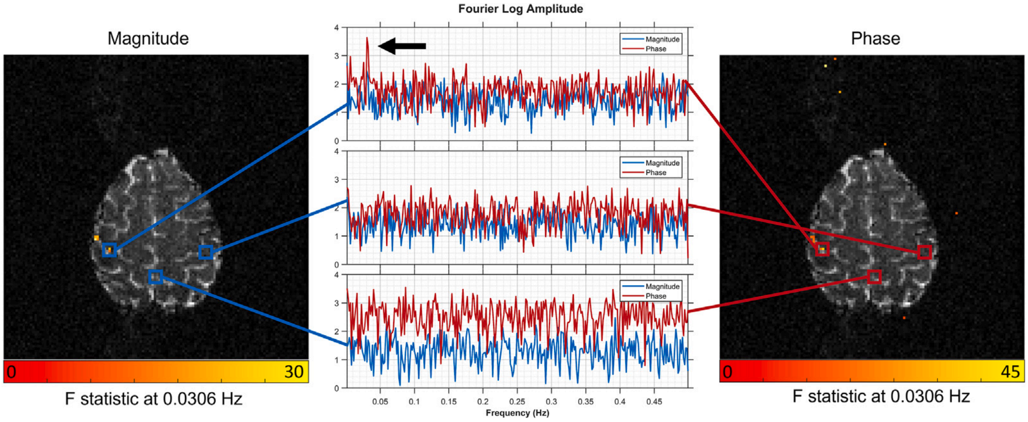

Fig. 10. Experimental data log Fourier coefficients (center) of the magnitude (blue) and phase (red) of voxels located in the left motor cortex (top), right motor cortex (middle), and posterior midline (bottom). The arrow in the top right plot indicates a large Fourier coefficient at a frequency of 19/621 s^{-1} or about 0.03 Hz. Left and right are the significant F-statistics for the magnitude- and phase-only Fourier coefficients, respectively. (For interpretation of the references to color in this figure legend, the reader is referred to the web version of this article.)

estimation model was tested on complex-valued simulated data and promising results were demonstrated on complex-valued experimental data. In both the simulated and experimental data it was demonstrated that the non-Normal Lathi distribution works well at all SNRs and has detected task-related phase changes in the left motor cortex from a unilateral right-handed finger tapping experiment. This mathematically correct model has stronger detection ability than the popular Normal assumption model. It also performs slightly better than a von Mises approximation.

Work has been done to show that the sensitivity of the phase data can contain physiologically meaningful and spatially distinct information [37–39], though the exact statistics may be different due to multiple coils and a more elaborate preprocessing pipeline. This work continues to show exciting results for the ability to detect additional biological information contained in the phase: task-related activation. This motivates further investigations into phase activation resulting from local magnetic field changes due to vascularity or even direct neuronal current [40–42].

CRediT authorship contribution statement

John C. Bodenschatz: Writing – original draft, Visualization, Software, Investigation, Formal analysis. **Daniel B. Rowe:** Writing – review & editing, Supervision, Resources, Project administration, Methodology, Formal analysis, Conceptualization.

Declaration of competing interest

None declared.

Appendix A. Power analysis of alternative distributions

In the hypothesis test described in Section 2 a significance level of $\alpha = 0.05$ was chosen. This represents the probability of committing a Type I error or false positive, which in this application would mean falsely claiming a voxel has some task-related phase change when in reality it does not. A result of fixing $\alpha = 0.05$ is the value of the power β of the hypothesis test. Statistical power is the ability of a hypothesis test to correctly reject the null hypothesis when it is false, or for this application, the probability of correctly identifying a voxel as having some task-related phase change. A depiction of statistical power is shown in Fig. A.1. In this figure, the maximum likelihood estimates of the parameters from an experimental voxel that was determined to be task-active are used to draw theoretical distributions. In black is the distribution for phase measurements under the null hypothesis that $\theta = \theta_0$. In red, blue, and green are the distributions for $\theta_0 + \theta_1$ under the alternative hypothesis that $\theta = \theta_0 + \theta_1 x_t$ using the mathematically correct Lathi distribution, the Normal approximation, and the von Mises approximation respectively. The power is represented by the similarly colored area under each $\theta_0 + \theta_1$ distribution curve, to the

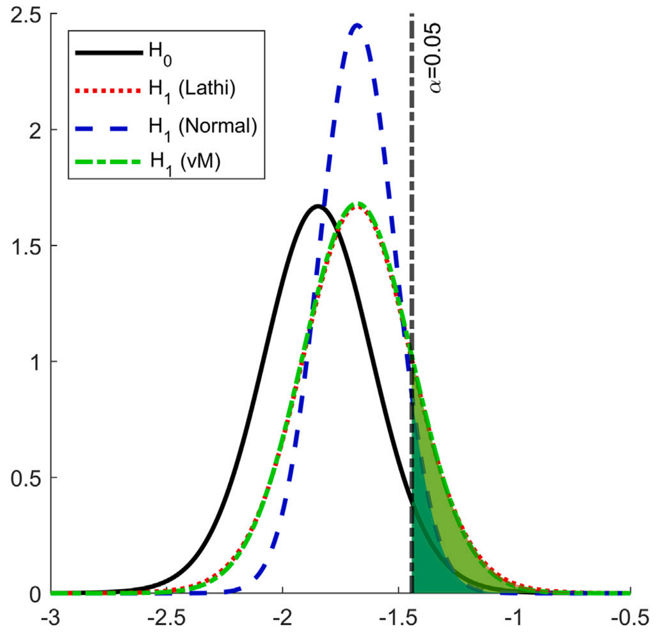

Fig. A.1. Theoretical distributions based on maximum likelihood estimates from an active voxel in Fig. 8. The null hypothesis (black) assumes the Lathi distribution in Eq. (6). The alternative hypothesis using the Lathi (red), Normal (blue), and von Mises (green) distributions. The power is the highlighted area to the right of the critical value for each alternative hypothesis distribution. (For interpretation of the references to color in this figure legend, the reader is referred to the web version of this article.)

right of the critical value θ_{0_α}. Here we can visually see that the Lathi distribution (red) and von Mises distribution (green) provide larger statistical power than the Normal assumption (blue) due to the large difference in area to the right of the critical value. The Lathi and von Mises distributions perform similarly.

The example in Fig. A.1 is for a specific voxel with an estimated value for θ_0 and $\theta_0 + \theta_1$. One way to generalize to other voxels is to vary the effect size (i.e. compare different values of θ_1) and observe how the power changes. This was done without loss of generality by using the estimate for θ_0 from the same voxel that was used for the previous example and adjusting the estimate for θ_1 from 0 to 1 radian. The power for each effect size is then calculated and plotted, resulting in Fig. A.2. The red, blue, and green power curves are for the alternative hypothesis following a Lathi, Normal, and von Mises distribution respectively. For effect sizes where $\theta_1 \lessapprox 0.5$ radians (about 30 degrees), the Lathi and von Mises distributions provide higher statistical power. The maximum likelihood estimate for θ_1 for the voxel from the active experimental voxel is marked by a vertical line at about 0.18. Measurements for θ_1 are observed to be at or below this level.

Note that this demonstrative example is for a one-tailed hypothesis test which assumes the phase change will be positive. The methods described in Section 2 support a two-tailed test, which is what is measured in practice in Section 3. This allows for the possibility of a negative change in phase, though it is observed that most changes are in the positive direction.

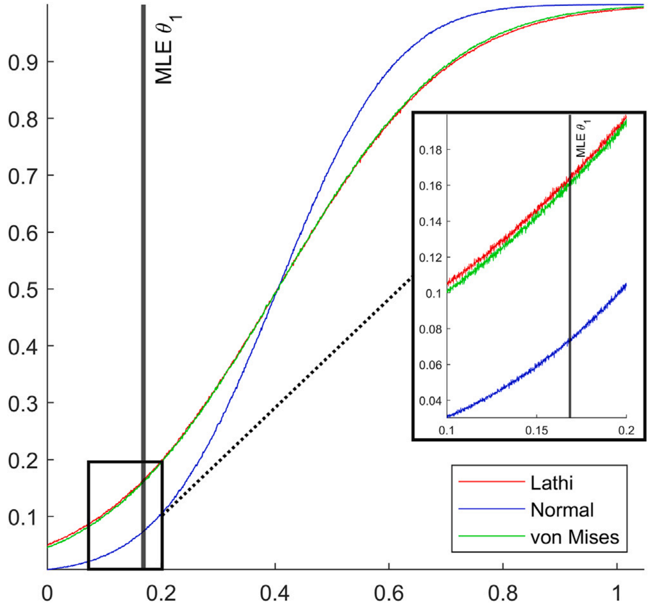

Fig. A.2. Power curves for Lathi (red), Normal (blue), and von Mises (green) alternative hypotheses under a null hypothesis that assumes the Lathi distribution in Eq. (6). The vertical line at about 0.18 indicates where the maximum likelihood estimate $\hat{\theta}_1$ was located for this particular active voxel. The inset image is a zoomed in region of interest to highlight the difference in statistical power of the three distributions. (For interpretation of the references to color in this figure legend, the reader is referred to the web version of this article.)

Appendix B. Experimental results for all seven slices

As mentioned in Section 3.2, the experimental data included seven axial slices. A particularly active slice was chosen for model demonstration in that section. Fig. B.1 shows a summary of results for all seven slices. The rows are organized by slice; slice 6 was examined in Section 3.2. The first column shows the maximum likelihood estimate for ρ for each slice. There is a small amount of Nyquist ghosting present in the magnitude estimation for each slice. The second and third columns show the estimates for θ_0 and θ_1 under the alternative hypothesis. Each baseline phase estimate $\hat{\theta}_0$ has some amount of phase wrapping that is known to cause issues when using simple linear estimation. The task-related phase change estimate $\hat{\theta}_1$ is visually similar for each slice when on the $[-\pi, \pi]$ scale. The fourth column is the variance estimation $\hat{\sigma}^2$. The final column are the Benjamini–Hochberg thresholded z-statistics superimposed onto anatomical magnitude images of the slices. The task-related phase change in the left motor cortex is most noticeable in

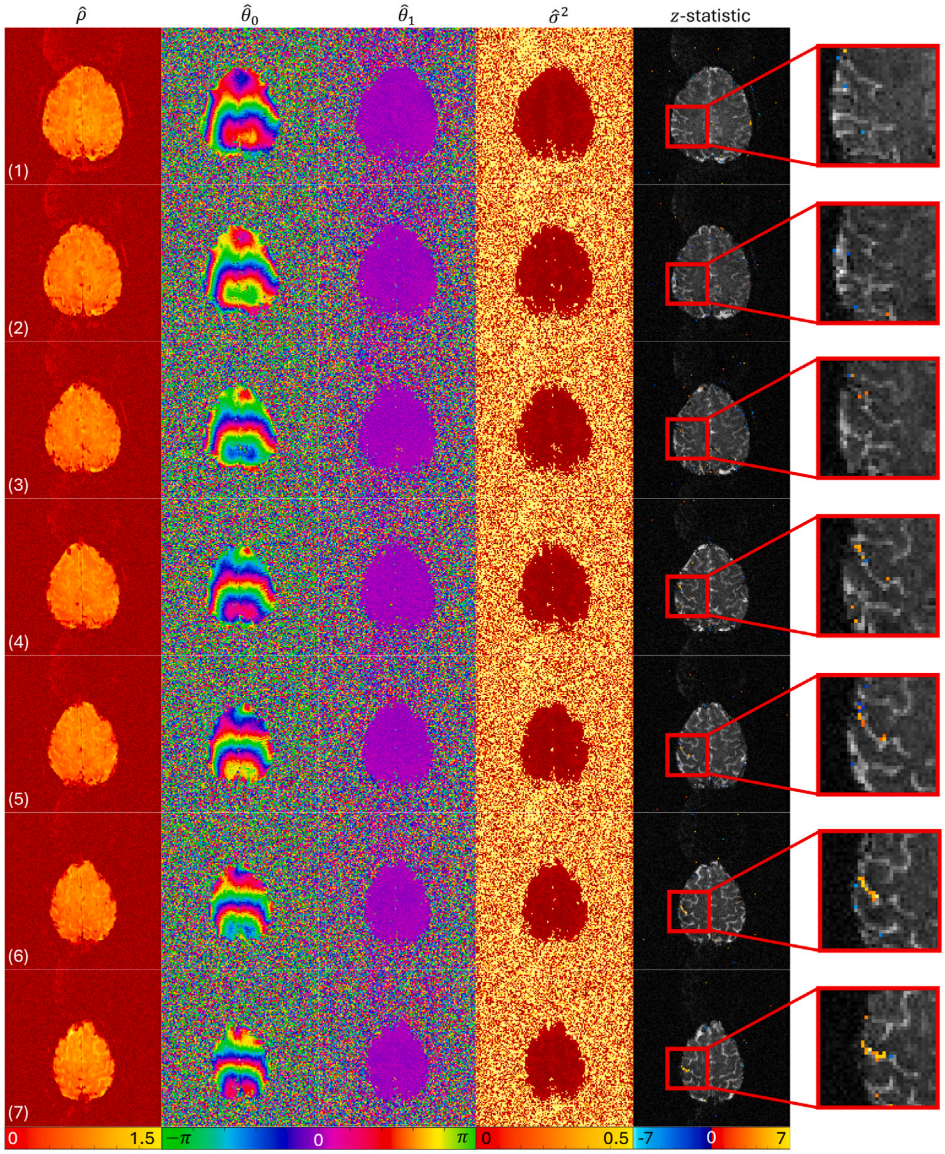

Fig. B.1. Summary images for all seven experimental slices (rows). The columns indicate magnitude estimation $\hat{\rho}$, baseline phase $\hat{\theta}_0$, task-related phase change $\hat{\theta}_1$, and variance $\hat{\sigma}^2$ under the alternative hypothesis, and $\alpha = 0.05$ thresholded z-statistics. Slice 6 was explored further in Section 3.2.

slices 6 (critical $z = 3.89$) and 7 (3.88), with trace amounts of activation detected in slices 4 (3.90) and 5 (3.90). Slices 1–4 exhibit no obvious signs of a task-related phase change.

References

[1] Kumar A, Welti D, Ernst RR. NMR Fourier zeugmatography. J Magn Reson 1975;18(1):69–83. http://dx.doi.org/10.1016/0022-2364(75)90224-3, (1969).

[2] Bernstein M, King K, Zhou X. Handbook of MRI pulse sequences. Elsevier Inc.; 2004, http://dx.doi.org/10.1016/B978-0-12-092861-3.X5000-6, Publisher Copyright: © 2004 Elsevier Inc. All rights reserved..

[3] Haacke EM. Magnetic resonance imaging: Physical principles and sequence design. 1999.

[4] Holland D, Kuperman JM, Dale AM. Efficient correction of inhomogeneous static magnetic field-induced distortion in echo planar imaging. NeuroImage 2010;50(1):175–83. http://dx.doi.org/10.1016/j.neuroimage.2009.11.044.

[5] Ogawa S, Lee TM, Kay AR, Tank DW. Brain magnetic resonance imaging with contrast dependent on blood oxygenation. Proc Natl Acad Sci USA 1990;87(24):9868–72. http://dx.doi.org/10.1073/pnas.87.24.9868.

[6] Bandettini PA, Jesmanowicz A, Wong EC, Hyde JS. Processing strategies for time-course data sets in functional MRI of the human brain. Magn Reson Med 1993;30(2):161–73. http://dx.doi.org/10.1002/mrm.1910300204.

[7] Chavhan GB, Babyn PS, Thomas B, Shroff MM, Haacke EM. Principles, techniques, and applications of T_2^*-based MR imaging and its special applications. RadioGraphics 2009;29(5):1433–49. http://dx.doi.org/10.1148/rg.295095034.

[8] Rowe DB. modeling both magnitude and phase of complex fMRI data. NeuroImage 2005;25:1310–24. http://dx.doi.org/10.1016/j.neuroimage.2005.01.034.

[9] Rowe DB. Parameter estimation in the magnitude-only and complex-valued fMRI data models. Neuroimage 2005;25(4):1124–32. http://dx.doi.org/10.1016/j.neuroimage.2004.12.048.

[10] Adrian DW, Maitra R, Rowe DB. Ricean over Gaussian modelling in magnitude fMRI analysis-added complexity with negligible practical benefits. Stat 2013;2(1):303–16. http://dx.doi.org/10.1002/sta4.34.

[11] Adrian DW, Maitra R, Rowe DB. Rice-distributed autoregressive time series modeling of magnitude functional MRI data. Ann Appl Stat 2025;19. http://dx.doi.org/10.1214/24-AOAS1981.

[12] Lai S, Glover GH. Detection of BOLD fMRI signals using complex data. Proc Int Soc Magn Reson Med 1997;1997(S1):1671. http://dx.doi.org/10.1002/mrmp.22419970134.

[13] Nan FY, Nowak RD. Generalized likelihood ratio detection for fMRI using complex data. IEEE Trans Med Imaging 1999;18(4):320–9. http://dx.doi.org/10.1109/42.768841.

[14] Rowe DB, Logan BR. A complex way to compute fMRI activation. Neuroimage 2004;23(3):1078–92. http://dx.doi.org/10.1016/j.neuroimage.2004.06.042.

[15] Rowe DB. Magnitude and phase signal detection in complex-valued fMRI data. Magnetic Reson Medicine 2009;62(5):1356–7; 1358–60. http://dx.doi.org/10.1002/mrm.21882.

[16] Adrian DW, Maitra R, Rowe DB. Complex-valued time series modeling for improved activation detection in fMRI studies. Ann Appl Statistics 2018;12(3):1451–78. http://dx.doi.org/10.1214/17-AOAS1117.

[17] Adrian DW, Maitra R, Rowe DB. Magnitude and phase activation detection in functional MRI time series. Proc Jt Stat Meet 2024. http://dx.doi.org/10.5281/zenodo.14010492.

[18] Yu C, Prado R, Ombao H, Rowe DB. A Bayesian variable selection approach yields improved detection of brain activation from complex-valued fMRI. J Amer Statist Assoc 2018;113(524):1395–410. http://dx.doi.org/10.1080/01621459.2018.1476244.

[19] Yu C-H, Prado R, Ombao H, Rowe D. Bayesian spatiotemporal modeling on complex-valued fMRI signals via kernel convolutions. Biometrics 2023;79(2):616–28. http://dx.doi.org/10.1111/biom.13631.

[20] Wang Z, Rowe DB, Li X, Brown DA. A fully Bayesian approach for comprehensive mapping of magnitude and phase brain activation in complex-valued fMRI data. Magn Reson Imaging 2024;109:271–85. http://dx.doi.org/10.1016/j.mri.2024.03.029.

[21] Wang Z, Rowe DB, Li X, Brown DA. Efficient fully Bayesian approach to brain activity mapping with complex-valued fMRI data. J Appl Stat 2025;52(6):1299–314. http://dx.doi.org/10.1080/02664763.2024.2422392.

[22] Rowe DB, Meller CP, Hoffmann RG. Characterizing phase-only fMRI data with an angular regression model. Journal Neurosci Methods 2007;161(2):331–41. http://dx.doi.org/10.1016/j.jneumeth.2006.10.024.

[23] Lathi B. Modern digital and analog communication. Oxford University Press; 1983.

[24] den Dekker AJ, Sijbers J. Implications of the rician distribution for fMRI generalized likelihood ratio tests. Magn Reson Imaging 2005;23(9):953–9. http://dx.doi.org/10.1016/j.mri.2005.07.008.

[25] Gudbjartsson H, Patz S. The rician distribution of noisy MRI data. Magn Reson Med 1995;34(6):910–4. http://dx.doi.org/10.1002/mrm.1910340618.

[26] Rowe DB. Statistics of intrinsic FMRI data. Proc Jt Stat Meet 2023. http://dx.doi.org/10.5281/zenodo.10002334.

[27] Rice SO. Mathematical analysis of random noise. Bell Syst Tech J 1944;23(3):282–332. http://dx.doi.org/10.1002/j.1538-7305.1944.tb00874.x.

[28] Rowe DB, Bodenschatz JC. Distributionally accurate FMRI phase activation. In: Proceedings of the joint statistical meeting. 2025, http://dx.doi.org/10.5281/zenodo.16921786.

[29] Wilks SS. The large-sample distribution of the likelihood ratio for testing composite hypotheses. Ann Math Stat 1938;9(1):60–2. http://dx.doi.org/10.1214/aoms/1177732360.

[30] Severini TA. Likelihood methods in statistics. In: Oxford statistical science series, London, England: Oxford University Press; 2000.

[31] Bodenschatz JC, Rowe DB. Simulation and harmonic analysis of k-space readout (SHAKER). 2025, URL https://arxiv.org/abs/2502.17620.

[32] Benjamini Y, Hochberg Y. Controlling the false discovery rate: A practical and powerful approach to multiple testing. J R Stat Soc Ser B Stat Methodol 1995;57(1):289–300. http://dx.doi.org/10.1111/j.2517-6161.1995.tb02031.x.

[33] Logan BR, Geliazkova MP, Rowe DB. An evaluation of spatial thresholding techniques in fMRI analysis. Hum Brain Mapp 2008;29(12):1379–89. http://dx.doi.org/10.1002/hbm.20471.

[34] Logan BR, Rowe DB. An evaluation of thresholding techniques in fMRI analysis. Neuroimage 2004;22(1):95–108. http://dx.doi.org/10.1016/j.neuroimage.2003.12.047.

[35] Nencka AS, Hahn AD, Rowe DB. A mathematical model for understanding the statistical effects of k-space (AMMUST-k) preprocessing on observed voxel measurements in fcMRI and fMRI. J Neurosci Methods 2009;181(2):268–82. http://dx.doi.org/10.1016/j.jneumeth.2009.05.007.

[36] Sakitis CJ, Rowe DB. Bayesian merged utilization of GRAPPA and SENSE (BMUGS) for in-plane accelerated reconstruction increases fMRI detection power. Magn Reson Imaging 2025;115:110252. http://dx.doi.org/10.1016/j.mri.2024.110252.

[37] Menon RS. Postacquisition suppression of large-vessel BOLD signals in high-resolution fMRI. Magn Reson Med 2002;47(1):1–9. http://dx.doi.org/10.1002/mrm.10041.

[38] Bandettini PA, Petridou N, Bodurka J. Direct detection of neuronal activity with MRI: Fantasy, possibility, or reality? Appl Magn Reson 2005;29(1):65–88. http://dx.doi.org/10.1007/BF03166956.

[39] Syväoja SS, Raitamaa L, Helakari H, Kantola J, Järvelä M, Kananen J, Isokoski V, Korhonen V, Väyrynen T, Tuovinen T, Hennig J, Kiviniemi V. Ultrafast complex-valued 4D fMRI reveals sleep-induced brain respiratory pulsation changes in both magnitude and phase signals. NeuroImage 2025;317:121290. http://dx.doi.org/10.1016/j.neuroimage.2025.121290.

[40] Shmuel A, Leopold DA. Neuronal correlates of spontaneous fluctuations in fMRI signals in monkey visual cortex: Implications for functional connectivity at rest. Hum Brain Mapp 2008;29(7):751–61. http://dx.doi.org/10.1002/hbm.20580.

[41] Harris JJ, Reynell C, Attwell D. The physiology of developmental changes in BOLD functional imaging signals. Dev Cogn Neurosci 2011;1(3):199–216. http://dx.doi.org/10.1016/j.dcn.2011.04.001.

[42] Mullinger K, Mayhew S, Bagshaw A, Bowtell R, Francis S. Evidence that the negative BOLD response is neuronal in origin: A simultaneous EEG–BOLD–CBF study in humans. NeuroImage 2014;94:263–74. http://dx.doi.org/10.1016/j.neuroimage.2014.02.029.